

Article

# Development of CO<sub>2</sub> Band-Based Cloud Emission and Scattering Indices and Their Applications to FY-3D Hyperspectral Infrared Atmospheric Sounder

Xinlu Xia  and Xiaolei Zou \*

Center of Data Assimilation for Research and Application, Nanjing University of Information Science & Technology, Nanjing 210044, China; stephenxia@nuist.edu.cn

\* Correspondence: xzou@nuist.edu.cn

Received: 27 November 2020; Accepted: 17 December 2020; Published: 19 December 2020



**Abstract:** The Hyperspectral Infrared Atmospheric Sounder (HIRAS) onboard the Feng Yun-3D (FY-3D) satellite is the first Chinese hyperspectral infrared instrument. In this study, an improved cloud detection scheme using brightness temperature observations from paired HIRAS long-wave infrared (LWIR) and short-wave infrared (SWIR) channels at CO<sub>2</sub> absorption bands (15- $\mu$ m and 4.3- $\mu$ m) is developed. The weighting function broadness and a set of height-dependent thresholds of cloud-sensitive-level differences are incorporated into pairing LWIR and SWIR channels. HIRAS brightness temperature observations made under clear-sky conditions during a training period are used to develop a set of linear regression equations between paired LWIR and SWIR channels. Moderate-resolution Imaging Spectroradiometer (MODIS) cloud mask data are used for selecting HIRAS clear-sky observations. Cloud Emission and Scattering Indices (CESIs) are defined as the differences in SWIR channels between HIRAS observations and regression simulations from LWIR observations. The cloud retrieval products of ice cloud optical depth and cloud-top pressure from the Atmospheric Infrared Sounder (AIRS) are used to illustrate the effectiveness of the proposed cloud detection scheme for FY-3D HIRAS observations. Results show that the distributions of modified CESIs at different altitudes can capture features in the distributions of AIRS-retrieved ice cloud optical depth and cloud-top pressure better than the CESIs obtained by the original method.

**Keywords:** CESIs; FY-3D HIRAS; LWIR and SWIR pair

## 1. Introduction

Hyperspectral infrared instruments onboard satellites have been a fundamental part of the earth observation system (EOS) since the twenty-first century. Owing to high spectral resolutions, high vertical resolution atmospheric profiles of temperature, humidity and cloud amount, water content, and cloud-top pressure can be retrieved [1–3]. The first hyperspectral infrared sounder is the 2378-channel Atmospheric Infrared Sounder (AIRS) onboard the National Aeronautics and Space Administration (NASA) Aqua satellite launched in May 2002 [4]. The second hyperspectral infrared sounder is the 8461-channel Infrared Atmospheric Sounding Interferometer (IASI) onboard the EUMETSAT Polar System's three polar-orbiting meteorological satellites MetOp-A/B/C [5,6]. The Cross-track Infrared Sounder (CrIS) is the third hyperspectral sounder onboard the Suomi National Polar-Orbiting Partnership (S-NPP) satellite launched in October 2011. CrIS is a hyperspectral Fourier transform spectrometer with 1305 channels at normal spectrum resolution (NSR) initially [7] and was been updated to 2211 channels at full spectrum resolution (FSR) on National Oceanic and Atmospheric Administration (NOAA)-20, which was launched in November 2017. The first Chinese hyperspectral infrared sounder is the Hyperspectral Infrared Atmospheric Sounder (HIRAS), which is a spaceborne

Fourier transform spectrometer with 2275 spectral channels. HIRAS has been onboard the FengYun-3D (FY-3D) satellite launched in November 2017 [8–10]. Observations from these hyperspectral infrared instruments have been used worldwide for numerical weather prediction (NWP) through data assimilation and climate research using retrieval products [1,11,12].

Atmospheric data assimilation is an important and complex process in NWP, in which the detection of cloud-contaminated satellite data is a key. Cloud detection methods can be broadly categorized into two categories: machine learning methods and classical algorithm-based methods. The machine learning techniques train forecast models by fusing model output with input samples to provide additional decision support [13,14] used an artificial neural net with many variations such as support vector machine, fusing multi-scale convolution features, deep learning, decision tree, Bayesian classification, etc. Machine learning methods are flexible because they simulate decisions on training data, but not consistent because model training depends on input data. Most classical algorithm-based methods used for cloud detection are based on thresholds, which are effective for different types of cloud but with poor universality [15]. Some of these generality issues have been overcome by statistical methods such as Principal Component Analysis [16]. Many researchers implement cloud detection techniques using physical parameters of clouds, such as shape attributes, the fusion of multi-scale convolutional features of the cloud net, color transformation, cloud density, cloud shadows, and clear-sky background differences [15]. Threshold methods identifying cloud-contaminated data directly based on brightness temperature differences have also been widely used in cloud detection and was applied to infrared imagers such as the Advanced Very High-Resolution Radiometer [17], the Moderate-resolution Imaging Spectroradiometer [18], and the Visible Infrared Imager Radiometer Suite [19]. By ranking the channels according to the channel sensitivity to clouds [20] developed a cloud detection method for AIRS observations selecting those channels whose weighting functions peak above the cloud top pressure for assimilation and eliminating lower-level channels in NWP models.

The CO<sub>2</sub> absorption at both LWIR (15- $\mu$ m) and SWIR (4.3- $\mu$ m) bands from hyperspectral infrared sounders provide a unique opportunity to detect clouds in different layers of the atmosphere. Because CO<sub>2</sub> is a uniformly mixed gas in the atmosphere, differences between LWIR and SWIR channels at similar altitudes provide information of cloud in addition to atmospheric temperatures at high vertical resolutions [21,22] developed a CO<sub>2</sub> slicing technique to determine cloud-top pressure according to the ratio of observations from two channels at CO<sub>2</sub> absorption bands (4.3- $\mu$ m, 15- $\mu$ m) that is suitable for cirrus cloud identification [23,24] used the CO<sub>2</sub> slicing technique to determine the cirrus cloud occurrence, height and effective emissivity with based on HIRS (High-resolution Infrared Radiation Sounder) observations. A new cloud detection scheme was recently proposed by [25] to define a set of the Cloud Emission and Scattering Indices (CESIs) for cloud detection by pairing CrIS LWIR and SWIR CO<sub>2</sub> channels. The algorithm is simple and can detect clouds in different vertical layers of the atmosphere. This study makes further improvements to this method and applies it to HIRAS observations from the FY-3D satellite. The concept of weighting function (WF) broadness is newly added, the threshold of the cloud-sensitive-level difference is made height-dependent when matching the LWIR and SWIR channels of HIRAS, the regression coefficients of CESIs are determined by HIRAS clear-sky observations. Cloud retrieval products from AIRS are used to demonstrate the effectiveness of the improved cloud detection scheme for HIRAS observations.

This paper is organized as follows. Section 2 describes the characteristics of HIRAS observations and channel characteristics. Section 3 gives details about the improved cloud detection scheme. In Section 4, results are provided to compare the actual effects of the improved and original cloud detection schemes when applied to HIRAS observations. Section 5 presents the summary and conclusions.

## 2. HIRAS Data Characteristics

The FY-3D satellite is one of the Chinese second-generation polar-orbiting meteorological satellite series. It was launched in November 2017 with an altitude of 830.5 km above the earth's surface, an orbital inclination angle of 98.6°, and a local equator-crossing time of 13:40. The HIRAS has been

onboard the FY-3D satellite since its launch. It is the first generation of Chinese hyperspectral infrared sounders, with 2275 spectral channels located in three spectral bands: the LWIR band from 650 to 1135  $\text{cm}^{-1}$ , the mid-wave infrared (MWIR) band from 1210 to 1750  $\text{cm}^{-1}$ , and the SWIR band from 2155 to 2550  $\text{cm}^{-1}$ . The spectral resolution of FSR HIRAS data is 0.625  $\text{cm}^{-1}$  for all channels. Along each scan line of HIRAS, there are 29 fields of regard (FORs) with two adjacent observation positions separated by  $3.6^\circ$ , and each FOR comprises an array of  $2 \times 2$  fields of view (FOVs). The view angle of each FOV is  $1.1^\circ$ , corresponding to a nadir spatial resolution of about 16 km. It takes 10 s to finish a single scan cycle. The swath width is 2250 km, corresponding to a range of scan angles from the nadir of  $\pm 50.4^\circ$ .

Due to the coefficient limitation provided by the Radiative Transfer for TOVS (RTTOV) [26,27], this study uses the NSR (0.625  $\text{cm}^{-1}$  for LWIR and 2.5  $\text{cm}^{-1}$  for SWIR channels) HIRAS data. Figure 1 shows the brightness temperature and peak WF altitudes for HIRAS LWIR (670–755  $\text{cm}^{-1}$ , 138 channels) and SWIR (2200–2400  $\text{cm}^{-1}$ , 81 channels) channels at  $\text{CO}_2$  bands simulated by RTTOV (version 12.3) model with the U.S. standard profile as input. The RTTOV model was developed by the European Centre for Medium-Range Weather Forecasts (ECMWF) [17,27]. Although the designed spectral distribution of the simulated HIRAS brightness temperature and peak WFs shown in Figure 1 are similar to CrIS channels [28], we find that brightness temperature observations of HIRAS SWIR channels with peak WFs above 200 hPa are noisy. Figure 2a provides an example for HIRAS SWIR channel 2007 with center frequency located at 2382.5  $\text{cm}^{-1}$ , and peak WF located at 133 hPa. Noise dominates the spatial distribution of HIRAS brightness temperature observations at this channel (Figure 2a). The spatial distribution of the CrIS SWIR channel with the same frequency (2382.5  $\text{cm}^{-1}$ , Figure 2b) is more reasonable and meaningful. For lower-level channels, noise does not dominate HIRAS observations (it still affects observations in high latitudes). Figure 2c,d show that brightness temperature observations of the HIRAS (Figure 2c) and CrIS (Figure 2d) SWIR channels with the same frequency at 2227.5  $\text{cm}^{-1}$  and peak WF at 535 hPa are similar, showing higher brightness temperatures in the tropics, higher brightness temperatures near nadir (scan angle is zero at nadir) than larger scan angles, and some cloud features with extremely low brightness temperature due to ice scattering. This problem of the HIRAS high-level channels has been reported to a relevant scientist of the HIRAS instrument development team at the China Meteorological Administration. In this study, SWIR channels with WF peaks above 200 hPa are not considered, limiting CESIs to below the 200-hPa altitude.

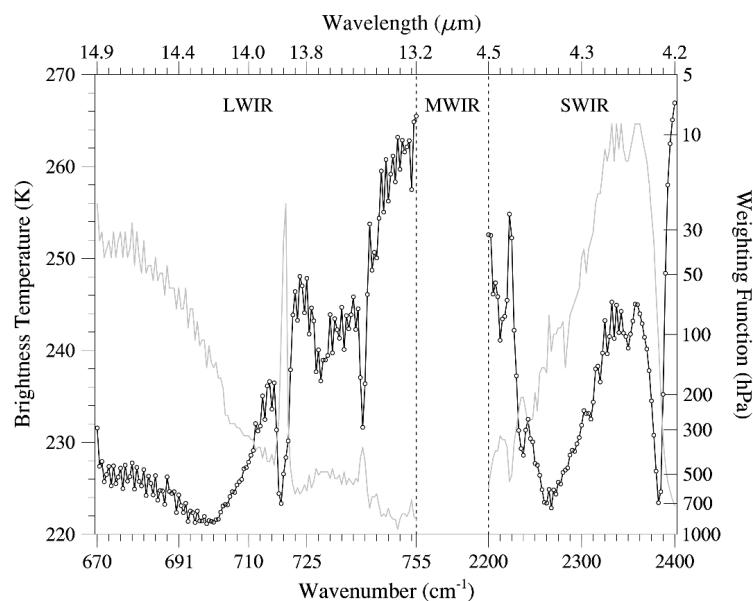


**Figure 1.** Radiative Transfer for TOVS (RTTOV) simulated brightness temperatures (black curves with open circle) and WF peaks (gray curves) for HIRAS LWIR and SWIR channels at  $\text{CO}_2$  bands using the U.S. standard profile.

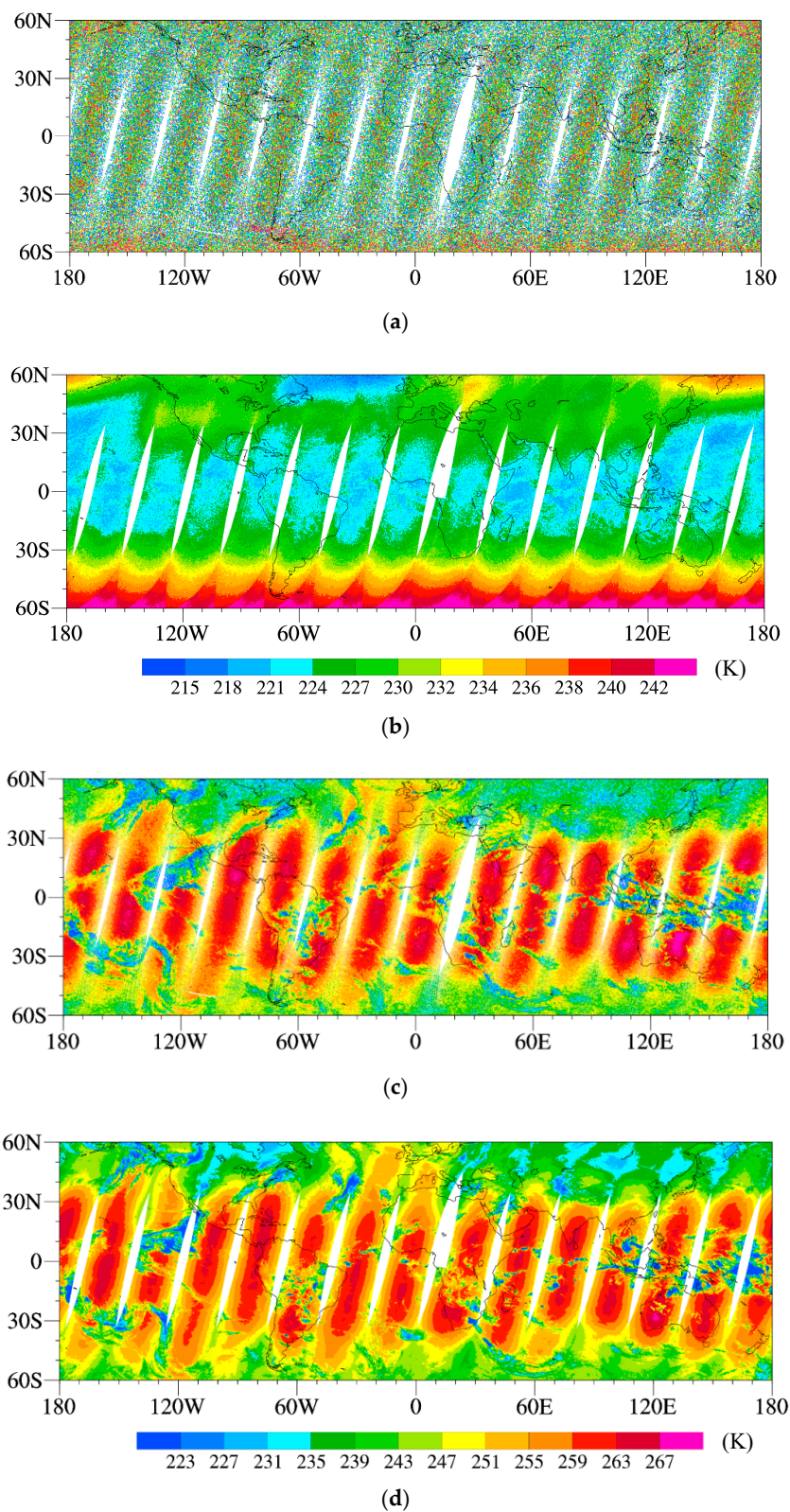


**Figure 2.** Spatial distributions of brightness temperature observations (unit: K) of (a) HIRAS SWIR channel 2007 ( $2382.5\text{ cm}^{-1}$ , peak WF at 133 hPa), (b) CrIS SWIR channel 1238 ( $2382.5\text{ cm}^{-1}$ , peak WF at 133 hPa), (c) HIRAS SWIR channel 1759 ( $2227.5\text{ cm}^{-1}$ , peak WF at 535 hPa), and (d) CrIS SWIR channel 1176 ( $2227.5\text{ cm}^{-1}$ , peak WF at 535 hPa) at descending nodes on 1 January 2019.

### 3. Description of the Modified Cloud Detection Scheme

Here, HIRAS LWIR (670–755  $\text{cm}^{-1}$ , 138 channels) and SWIR (2200–2400  $\text{cm}^{-1}$ , 81 channels) channels at  $\text{CO}_2$  bands are paired using the cloud detection method of [25] with modifications. The new method consists of the following three sequential steps: Step 1 pairs LWIR channels with SWIR channels based on WF profiles; step 2 selects the LWIR and SWIR channels paired in step 1, based on similar cloud-sensitive levels and minimum root mean square error (RMSE) between them; and step 3 finally calculates the CESIs. Details are given next.

#### 3.1. Pairing LWIR and SWIR Channels Based on WFs

For each LWIR channel and its paired SWIR channel, the difference between their peak WFs ( $\Delta p^{WFpeak}$ ) should be the same or less than 50 hPa, i.e.,

$$\Delta p^{WFpeak} = \left| p_{LW}^{WFpeak} - p_{SW}^{WFpeak} \right| \leq 50 \text{ hPa}, \quad (1)$$

where  $\Delta p_{LW}^{WFpeak}$  and  $\Delta p_{SW}^{WFpeak}$  are determined based on the WF profiles simulated by the RTTOV model with the U.S. standard profile as input. This was the only criterion used by original method in step 1. In fact, a single LWIR channel could be paired with several SWIR channels under the criterion expressed by Equation (1).

Figure 3 shows an example where LWIR channel 143 (13.5  $\mu\text{m}$ ) is paired with three SWIR channels, i.e., channels 2023 (4.18  $\mu\text{m}$ ), 1715 (4.54  $\mu\text{m}$ ), and 1751 (4.5  $\mu\text{m}$ ). The WF profiles of SWIR channels 1715, and 1751 are much different from SWIR channel 2023 and LWIR channel 143. So, we propose adding another criterion based on the broadness ( $B$ ) of the WFs (Figure 4):

$$\Delta B = |B_{LW} - B_{SW}| \leq 200 \text{ hPa} \quad (2)$$

where  $B_{LW}$  and  $B_{SW}$  are the broadness of the WFs of the LWIR and SWIR channels paired by Equation (1). Their values are determined by the following constraints:

$$B_{LW} = p_{1,LW} - p_{2,LW}, \quad B_{SW} = p_{1,SW} - p_{2,SW}, \quad (3)$$

$$W(p_{2,LW}) = W(p_{2,SW}), \quad W(p_{2,SW}) = W(p_{1,SW}), \quad (4)$$

$$\frac{\int_{p_{1,LW}}^{p_{2,LW}} W_{LW} d(\ln p)}{\int_{p_s}^0 W_{LW} d(\ln p)} = \frac{3}{4}, \quad \frac{\int_{p_{1,SW}}^{p_{2,SW}} W_{SW} d(\ln p)}{\int_{p_s}^0 W_{SW} d(\ln p)} = \frac{3}{4}, \quad (5)$$

where  $W_{LW}$  and  $W_{SW}$  are the WFs of the LWIR and SWIR channels, respectively,  $p_{1,LW}(p_{1,SW})$  and  $p_{2,LW}(p_{2,SW})$  are the lower and upper boundaries of the area satisfying Equation (5) for the LWIR (SWIR) channel, and  $p_s$  is the surface pressure. Equation (5) is based on the work by [29]. Figure 4 illustrates the areas satisfying Equation (3) of LWIR channel 143 and SWIR channel 1751, accounting for three-quarters of the total area surrounded by the  $y$ -axis and the corresponding WFs. For the example shown in Figure 3, only SWIR channel 2023 meets the criteria set by Equations (2)–(5), so that the other two SWIR channels, i.e., channels 1715 and 1751 are eliminated by the newly added criterion on WF broadness in step 1.

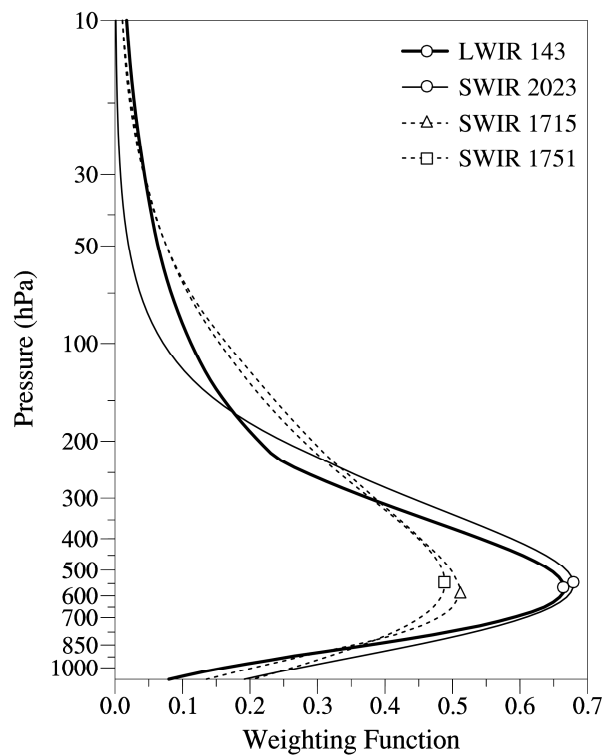


**Figure 3.** WF profiles (curves) and WF peaks (symbols) of LWIR channel 143 (thick solid curve with open circles) and four SWIR channels satisfying the criterion: 2023 (thin solid curve with open circles), 1715 (dashed curve with triangles), and 1751 (dashed curve with squares).

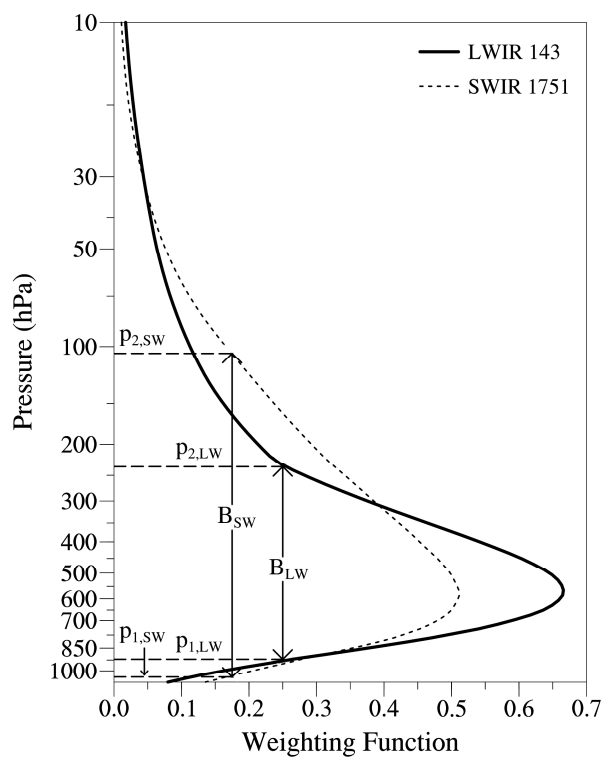


**Figure 4.** The WF broadness  $B_{LW} = p_{1,LW} - p_{2,LW}$  and  $B_{SW} = p_{1,SW} - p_{2,SW}$  for LWIR channel 143 (solid curve) and SWIR channel 1751 (dashed curve). The difference of WF broadness  $\Delta B = |B_{LW} - B_{SW}|$  between LWIR channel 143 and SWIR channels 2023, 1715 and 1751, whose WFs are shown in Figure 3, is 86, 227 and 255 hPa, respectively.

### 3.2. Pairing LWIR and SWIR Channels with Similar Cloud-Sensitive Levels and Minimum RMSE

The cloud-sensitive levels are determined by the following equations [20]:

$$\left| \frac{R_{LW}^{cloud} - R_{LW}^{clear}}{R_{LW}^{clear}} \right|_{p_{CS,LW}} \leq 0.01, \quad \left| \frac{R_{SW}^{cloud} - R_{SW}^{clear}}{R_{SW}^{clear}} \right|_{p_{CS,SW}} \leq 0.1 \quad (6)$$

where  $R_{LW}^{clear}$  ( $R_{SW}^{clear}$ ) represents the RTTOV-simulated radiances of the LWIR (SWIR) channel under clear-sky conditions, and  $R_{LW}^{cloud}$  ( $R_{SW}^{cloud}$ ) represents the RTTOV-simulated radiances of the LWIR (SWIR) channel with an opaque cloud (as a blackbody which fills the radiometer field of view) located at pressure level  $p_L$ . As  $p_L$  varies from 150 hPa to the surface, the fractional differences in radiance between cloudy and clear-sky simulations, i.e., the left-hand sides of the two equations in (6), are calculated until they meet the criteria set by Equation (6). The values of  $p_L$  that satisfy Equation (6) are defined as the cloud-sensitive levels, denoted as  $p_{CS,LW}$  and  $p_{CS,SW}$  for LWIR and SWIR channels, respectively. The thresholds for LWIR (0.01) and SWIR (0.1) in Equation (6) are determined empirically based on their noise level and cloud sensitivity. The impacts of clouds below the cloud-sensitive levels are very small and can be neglected. The difference in cloud-sensitive levels between LWIR and SWIR channels,  $\Delta p_{CS} = p_{CS,LW} - p_{CS,SW}$ , is used for further screen. The original method set a fixed threshold for  $|\Delta p_{CS}|$  as 50 hPa. We find that this threshold works well for channels whose peak WFs are located in the lower troposphere. However, for channels whose peak WFs are located in the upper levels of the atmosphere, the 50-hPa threshold is not strict enough. In this study, a set of height-dependent thresholds for  $|\Delta p_{CS}|$  are proposed and used for pairing LWIR and SWIR channels in this step, and in the meantime the brightness temperature RMSE between the chosen LWIR and SWIR channels should be minimum.

Figure 5 shows a flow chart summarizing the major procedures involved in pairing the HIRAS LWIR and SWIR channels described above.

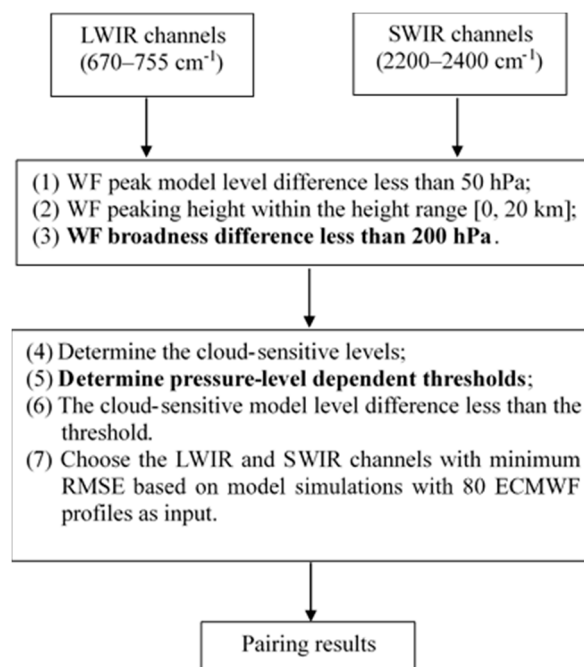


**Figure 5.** Flow chart summarizing three major steps in the HIRAS LWIR/SWIR pairing procedure. Modifications added in this study to original method are indicated in bold.

### 3.3. Calculating the CESI

Having obtained the paired LWIR and SWIR channels, a linear regression model of brightness temperature observations between LWIR and SWIR channels of each pair is established:

$$T_{b,regression}^{SWIR} = \alpha T_b^{LWIR} + \beta \quad (7)$$

where  $T_{b,regression}^{SWIR}$  is the modeled SWIR brightness temperature, and  $T_b^{LWIR}$  represents the observed LWIR brightness temperature. In the original method, simulated brightness temperature was used as  $T_b$  to calculate the regression coefficients with 50 ECMWF profiles as input for model. In this study, HIRAS brightness temperature observations under clear-sky condition are used as  $T_b$  for regression calculation. This approach avoids the simulation errors caused by profiles and ensures a sufficient amount of data for regression. The regression coefficients  $\alpha$  and  $\beta$  are derived by minimizing the sum of the squares of the deviations between HIRAS LWIR and SWIR observations:

$$\min_{\alpha, \beta} \left( \sum_{i=1}^n (T_{b,SW,i}^{obs,clear} - \alpha T_{b,LW,i}^{obs,clear} - \beta)^2 \right) \quad (8)$$

where the subscript “ $i$ ” represents an index for summation over a data sample. HIRAS brightness temperature observations under clear-sky condition are selected based on the collocation with MYD035 cloud mask products (retrieved from MODIS). MODIS is a 36-band spectroradiometer measuring visible and infrared radiation, whose retrievals have been widely applied to cloud detection [30]. The MODIS instruments were launched onboard the Terra and Aqua satellites in December 1999 and May 2002, respectively. Aqua is part of the A-train constellation of EOS satellites, which flies in a polar orbit at 705 km. The local equator-crossing time of the Aqua satellite is 13:30, which is close to that of the FY-3D satellite (13:40). The MYD035 cloud mask product has a 5-km resolution, which is higher than the 16-km resolution (at nadir) of HIRAS observations. Thus, HIRAS clear-sky observation is determined as: all collocated MYD035 cloud mask products within the HIRAS observation FOV are clear. The collocation criterion on the observation time difference between HIRAS and MODIS is less than 16 min (Section 4.2).

When the linear relationships of each paired LWIR/SWIR channels are obtained, the CESI can be finally defined as

$$CESI = T_{b,SW}^{reg}(T_{b,LW}^{obs}, \alpha, \beta) - T_{b,SW}^{obs} = (\alpha T_{b,LW}^{obs} + \beta) - T_{b,SW}^{obs}. \quad (9)$$

In the presence of ice particles, the cloud-top emission and scattering intensities between LWIR channel (15- $\mu\text{m}$ ) and SWIR channel (4.3- $\mu\text{m}$ ) at  $\text{CO}_2$  bands are different. Based on brightness temperature observations, we find that the cooling effect on SWIR channel is more significant if ice clouds exist. Therefore, CESIs reflect the intensity of cooling for SWIR channels which can be used to determine whether there are ice clouds at different altitudes. Similar CESI cloud detection algorithms have been applied to the microwave temperature sounder and the humidity sounder [31].

## 4. Results

### 4.1. Pairing HIRAS LWIR and SWIR Channels

Table 1 lists the total number of LWIR and SWIR pairs selected by original (second column) and modified (third column) method described in Section 3.1 after step 1, respectively. The peak WFs of the paired channels are distributed from about 250 hPa to 775 hPa, and the number of paired channels decreases significantly when adding the criterion based on the WF broadness in this study.

**Table 1.** Number of LWIR and SWIR pairs selected from channels at CO<sub>2</sub> bands of HIRAS within different pressure layers by original method (second column) and when adding the criterion based on the WF broadness in this study (third column) after step 1.

Pressure (hPa)	Number	Number
250–275	25	22
275–300	48	33
300–325	33	14
325–350	18	6
350–375	44	21
375–400	13	7
400–425	10	9
425–450	6	6
450–475	12	6
475–500	15	7
500–525	12	7
525–550	32	14
550–575	20	17
575–600	8	8
600–625	6	6
625–650	9	6
650–675	6	4
700–725	2	2
725–750	2	2
750–775	1	1

In step 2, a set of sensitivity experiments is carried out by changing  $|\Delta p_{CS}|$  on different pressure levels and we obtain a set of height-dependent thresholds for the cloud-sensitive-level differences between the LWIR and SWIR channels to be paired. In the meantime, 80 ECMWF profiles [32] are used as input for RTTOV model simulations of brightness temperature to calculate the RMSEs between paired LWIR and SWIR channels. Both the cloud-sensitive-level difference and brightness temperature RMSE between the final chosen LWIR/SWIR channels should be minimum. Table 2 shows the differences of WF peak, WF broadness, cloud-sensitive level and the RMSE between the finally paired LWIR and SWIR HIRAS channels during these two pairing steps discussed above.

**Table 2.** Pair number, differences of the WF peak ( $\Delta p^{WFpeak}$ ), WF broadness ( $\Delta P^{broadness}$ ), cloud-sensitive level ( $\Delta p_{CS}$ ) and the RMSE between the finally paired LWIR and SWIR HIRAS channels during two pairing steps.

Pair	Step 1		Step 2	
	$\Delta p^{WFpeak}$ (hPa)	$\Delta P^{broadness}$ (hPa)	$\Delta p_{CS}$ (hPa)	RMSE (K)
1	12	28	23	11.5
2	25	0	16	9.8
3	38	0	18	8.6
4	27	74	14	9.2
5	38	51	10	8.6
6	42	31	19	9.4
7	0	32	6	11.3
8	45	101	46	13.6
9	48	78	36	12.8
10	35	19	5	15.8
11	17	44	1	15.3
12	0	11	33	15.0
13	18	3	6	15.1
14	37	34	32	13.7
15	0	107	3	12.8
16	19	186	16	12.1

Table 2. Cont.

Pair	Step 1		Step 2	
	$\Delta p^{WFpeak}$ (hPa)	$\Delta p^{broadness}$ (hPa)	$\Delta p_{CS}$ (hPa)	RMSE (K)
17	40	178	1	9.0
18	20	162	7	8.3
19	40	134	4	11.0
20	0	57	9	14.3
21	22	57	1	14.1
22	44	134	6	14.7
23	0	180	8	8.9
24	0	39	26	12.5
25	23	66	11	11.9
26	47	158	35	5.8

A total of 26 paired HIRAS LWIR/SWIR channels are obtained by the modified method and their characteristics can be seen in Table 3. And we also pair HIRAS LWIR/SWIR channels by the original method, obtaining 24 pairs with their characteristics in Table 4. Among the results obtained by these two methods, 12 pairs are exactly the same. The modified method provides channels with peak WFs located at the middle troposphere (pair 8 and 9) which original method cannot.

**Table 3.** Channel number, wavenumber, WF peak and cloud-sensitive level ( $p_{CS}$ ) for the final paired 26 LWIR an SWIR HIRAS channels using the modified method in this study.

Pair	LWIR				SWIR			
	Channel Number	Wave-Number (cm <sup>-1</sup> )	Peak WF (hPa)	$p_{CS,LW}$ (hPa)	Channel Number	Wave-number (cm <sup>-1</sup> )	Peak WF (hPa)	$p_{CS,SW}$ (hPa)
1	88	704.375	253	368	1799	2252.500	241	391
2	111	718.750	266	407	1799	2252.500	241	391
3	91	706.250	279	409	1799	2252.500	241	391
4	94	708.125	293	440	1791	2247.500	266	454
5	95	708.750	307	444	1791	2247.500	266	454
6	98	710.625	321	501	1783	2242.500	279	520
7	99	711.250	336	509	2015	2387.500	336	503
8	105	715.000	366	640	1735	2212.500	321	716
9	108	716.875	399	652	1759	2227.500	351	718
10	146	740.625	415	705	2019	2390.000	450	710
11	107	716.250	433	709	2019	2390.000	450	710
12	109	717.500	450	677	2019	2390.000	450	710
13	127	728.750	468	704	2019	2390.000	450	710
14	131	731.250	487	678	2019	2390.000	450	710
15	124	726.875	506	827	1755	2225.000	506	830
16	136	734.375	525	814	1755	2225.000	506	830
17	142	738.125	545	814	1715	2200.000	585	815
18	140	736.875	565	822	1715	2200.000	585	815
19	125	727.500	585	846	1751	2222.500	545	850
20	123	726.250	606	867	2027	2395.000	606	876
21	120	724.375	628	875	2027	2395.000	606	876
22	151	743.750	650	870	2027	2395.000	606	876
23	168	754.375	672	897	2031	2397.500	672	889
24	154	745.625	718	923	2035	2400.000	718	897
25	150	743.125	741	908	2035	2400.000	718	897
26	167	753.750	765	932	2035	2400.000	718	897

**Table 4.** Same as Table 3 except for the 24 pairs using the original method.

Pair	LWIR				SWIR			
	Channel Number	Wave-Number (cm <sup>-1</sup> )	Peak WF (hPa)	$p_{CS,LW}$ (hPa)	Channel Number	Wave-Number (cm <sup>-1</sup> )	Peak WF (hPa)	$p_{CS,SW}$ (hPa)
1	88	704.375	253	368	1799	2252.500	241	391
2	111	718.750	266	407	1799	2252.500	241	391
3	91	706.250	279	409	1799	2252.500	241	391
4	94	708.125	293	440	1791	2247.500	266	454
5	95	708.750	307	444	1791	2247.500	266	454
6	98	710.625	321	501	1783	2242.500	279	520
7	99	711.250	336	509	2015	2387.500	336	503
8	146	740.625	415	705	2019	2390.000	450	710
9	107	716.250	433	709	1732	2205.000	415	758
10	109	717.500	450	677	2019	2390.000	450	710
11	116	721.875	468	741	2019	2390.000	450	710
12	139	736.250	487	797	1719	2202.500	487	840
13	124	726.875	506	827	1719	2202.500	487	840
14	133	732.500	525	819	1719	2202.500	487	840
15	145	740.000	545	778	1715	2200.000	585	815
16	143	738.750	565	826	1715	2200.000	585	815
17	125	727.500	585	846	1715	2200.000	585	815
18	149	742.500	606	865	1715	2200.000	585	815
19	153	745.000	628	825	1715	2200.000	585	815
20	151	743.750	650	870	2027	2395.000	606	876
21	168	754.375	672	897	2031	2397.500	672	889
22	154	745.625	718	923	2031	2397.500	672	889
23	158	748.125	741	925	2035	2400.000	718	897
24	167	753.750	765	932	2035	2400.000	718	897

Figure 6 shows the distributions of their peak WFs with pressure respectively, which can provide information of the atmosphere about around 240 hPa to 760 hPa. The WF broadness comparison between the paired LWIR and SWIR channels derived from these two methods are shown in Figure 7. For pairs on the same pressure level, the broadness difference between LWIR and SWIR channels obtained by modified method is generally smaller. In other words, LWIR/SWIR channels obtained by modified method can provide more detailed atmosphere information.

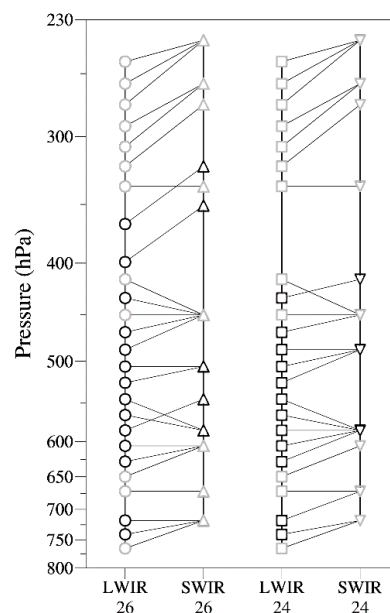


**Figure 6.** Vertical distribution of LWIR (circle and square) and SWIR (upward-pointing triangle and downward-pointing triangle) peak WF of 26 (modified method) and 24 (original method) pairs. Grey markers indicate the same paired LWIR and SWIR channels.

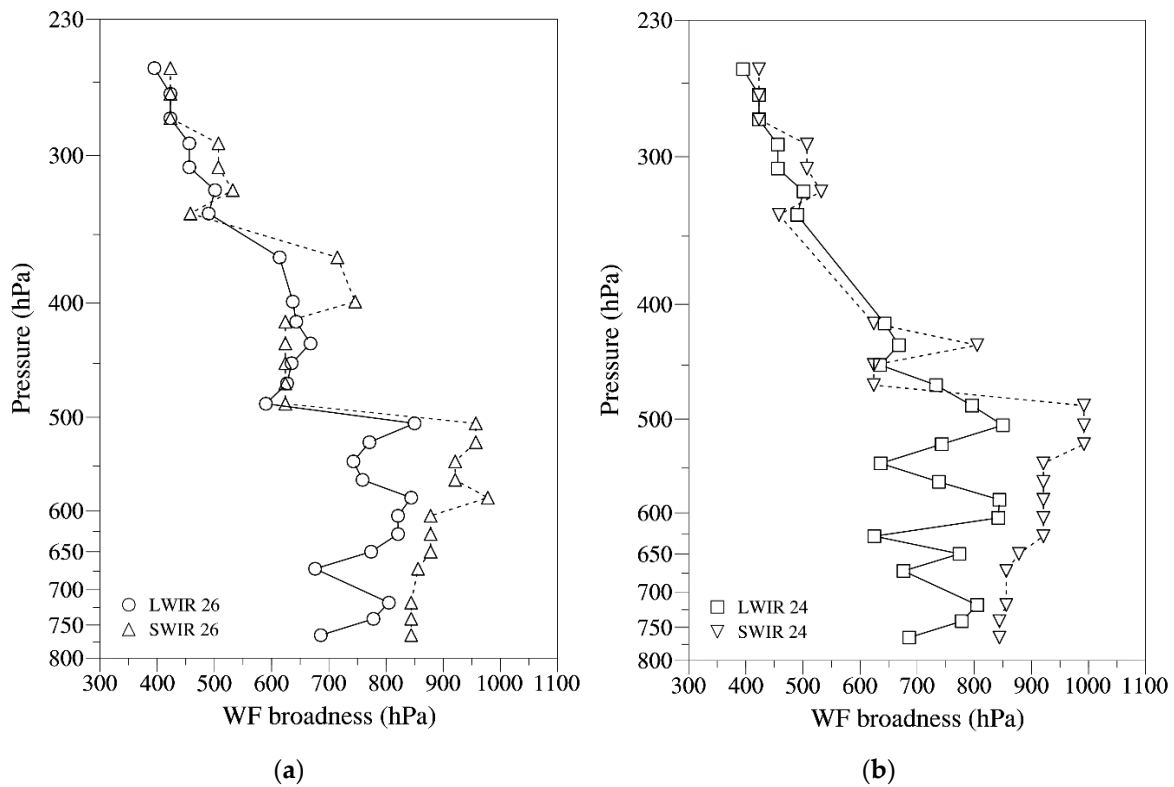


**Figure 7.** Vertical distribution of WF broadness for (a) modified method's 26 pairs and (b) original method's 24 pairs.

4.2. HIRAS CESIs

Before calculating the regression coefficients for CESIs, we need to select clear-sky HIRAS observations by collocating with MYD035 cloud mask products. The HIRAS clear-sky observation is determined as: all collocated MYD035 cloud mask products (5-km resolution) within the HIRAS observation FOV (16-km resolution at nadir) are clear. Figure 8a,b show the local time distributions of MODIS (tracks indicated by dashed curves) and HIRAS (tracks indicated by solid curves) observations from ascending nodes during 0000–2400 UTC 1 January 2019. Their local equator-crossing times are very close and the distribution of time difference between them from ascending and descending nodes on 1 January 2019 are shown in Figure 8c,d, respectively.

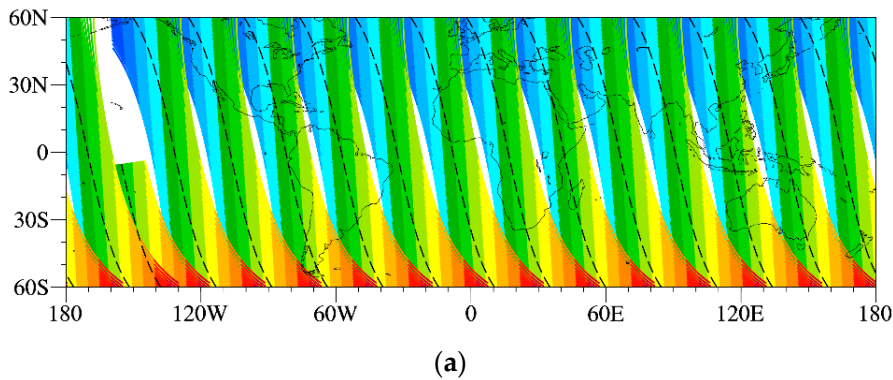


**Figure 8.** Cont.

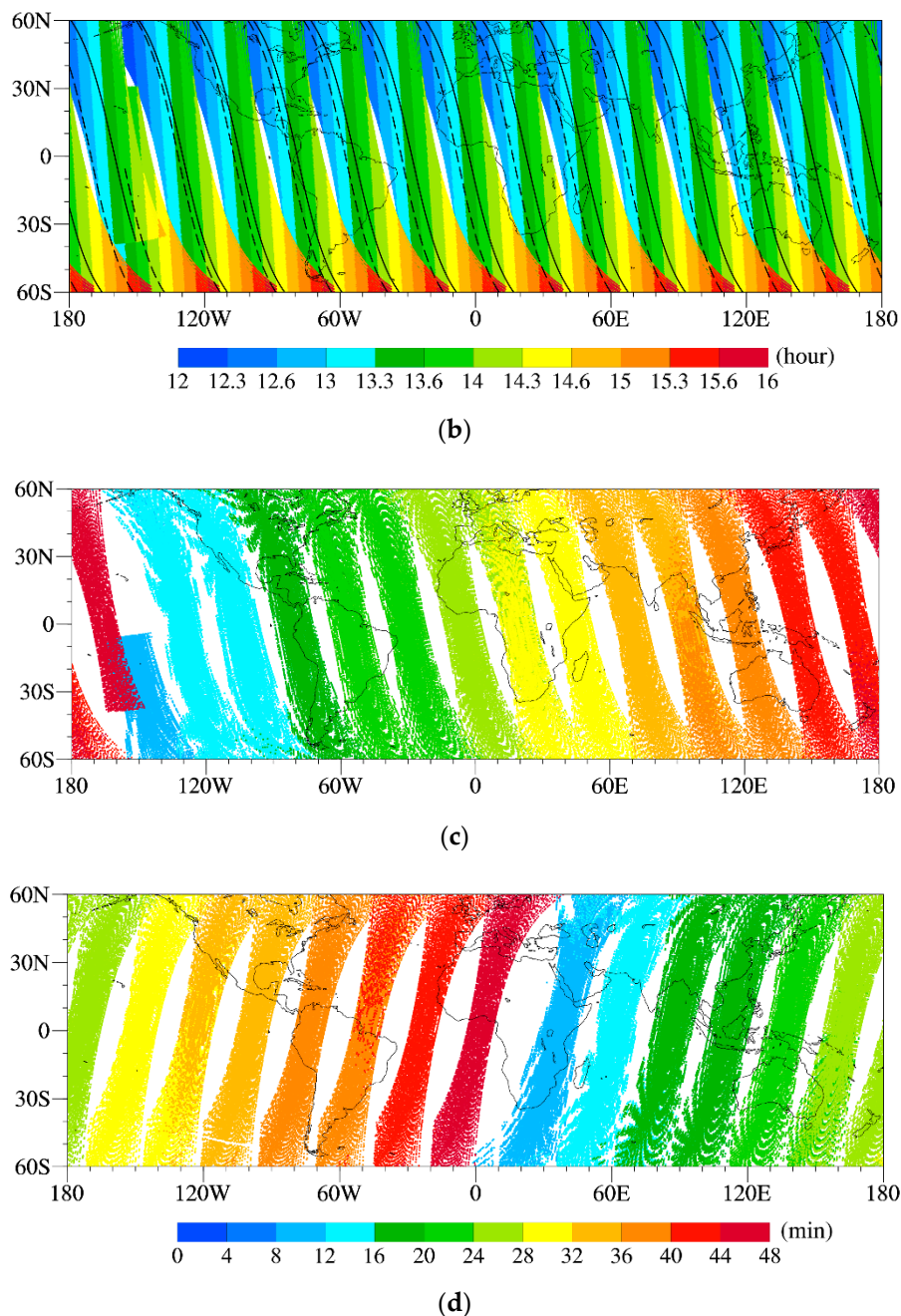


**Figure 8.** Local time distributions of (a) MODIS and (b) HIRAS from ascending nodes and time difference between them from (c) ascending nodes and (d) descending nodes during 0000–2400 UTC 1 January 2019. The black lines in (b) are the tracks of the MODIS (dashed) and HIRAS (solid).

While ensuring enough data volume, the clear-sky selection will be more accurate if the observation time difference is smaller. Based on the discussion above, the collocation criterion on the observation time difference between HIRAS and MODIS data used in this study is less than 16 min. In this study, MYD035 cloud mask products from 1–20 January 2019 are used for collocating HIRAS clear-sky observations. Figure 9a takes an example of a regional distribution of the MYD035 cloud mask products from descending nodes on 1 January 2019, with bright green dots showing matched HIRAS clear-sky observations. Take pair 6 in Table 3 (LWIR 98, SWIR 1783) as an example, these HIRAS clear-sky observations are picked out and plotted as a scatter plot in Figure 9b. It can be seen that there is a good linear relationship between the clear-sky brightness temperature of LWIR and SWIR channels. Scatter

shown in Figure 9c are HIRAS cloudy observations picked out from this area. As can be seen from this figure, in the presence of clouds, there is a more pronounced drop in brightness temperature of SWIR channel than LWIR channel which is consistent with the statement in Section 3.3.

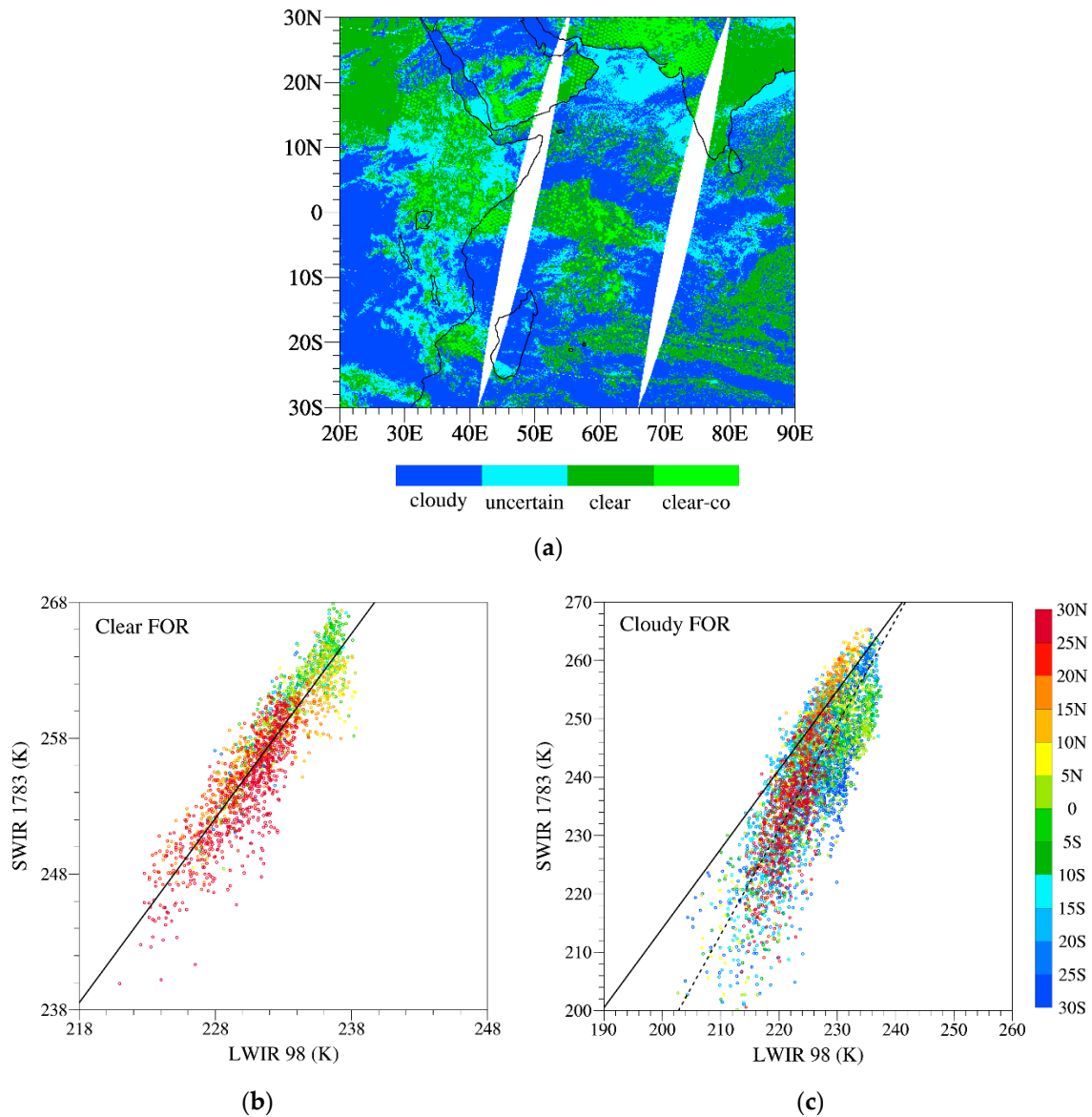


**Figure 9.** Distribution of the (a) MOD035 cloud mask at a 5-km resolution at descending node on January 1. Bright green dots are collocated HIRAS clear-sky observations. Scatter plots of HIRAS brightness temperature of LWIR 98 and SWIR 1783 are from (b) clear-sky and (c) cloudy observations in this area. Black lines indicate the linear regression between LWIR and SWIR brightness temperature under clear-sky condition (solid) and cloudy condition (dashed).

Considering the scan-dependent feature of HIRAS observed brightness temperature, all 29 HIRAS FORs of each pair are used for regression respectively. The CESI regression coefficients of  $\alpha$  and  $\beta$  for 26 pairs (modified method) and 24 pairs (original method) are shown in Figures 10 and 11, respectively, and these coefficients vary regularly with the scan angle. When all pairs of CESIs from both modified and original methods are obtained, they can be used for cloud detection comparison.

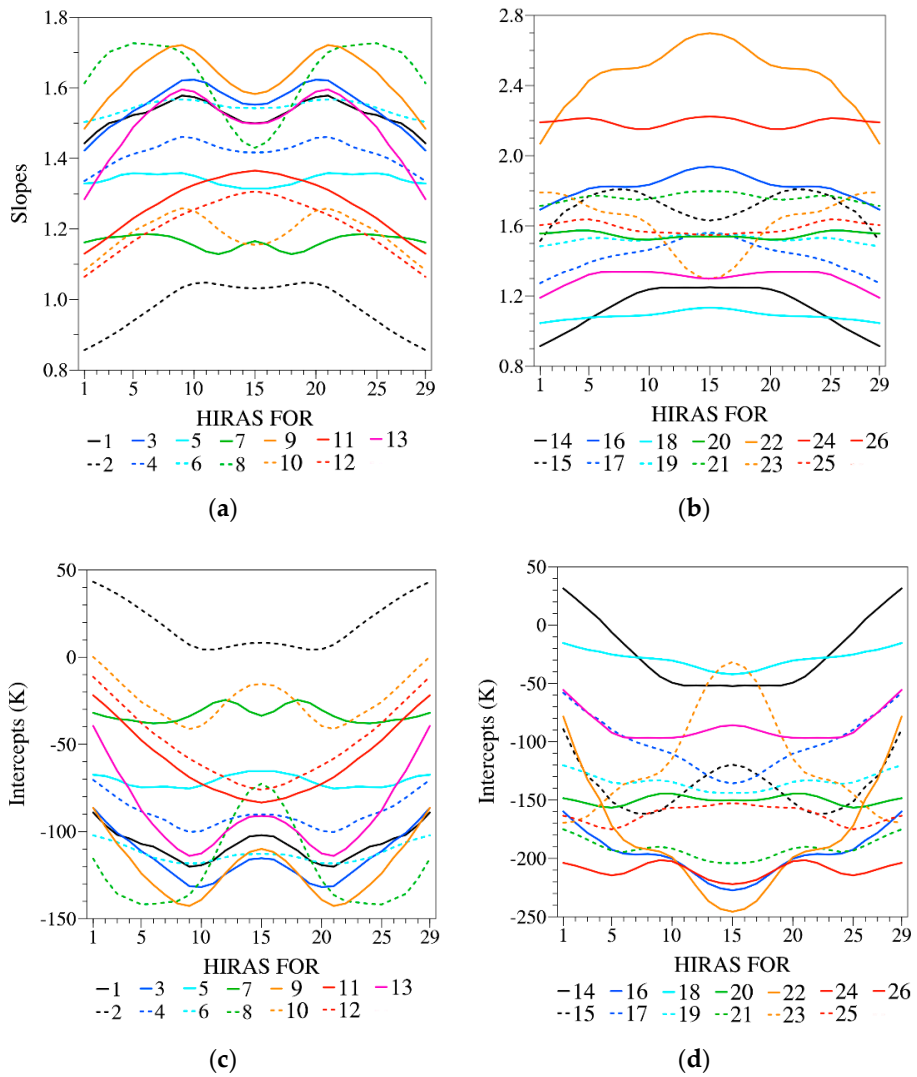


**Figure 10.** Regression coefficients (a,b)  $\alpha$  and (c,d)  $\beta$  of the linear regression model ( $T_{b,regression}^{SWIR} = \alpha T_{obs}^{LWIR} + \beta$ ) for 29 FORs of the 26 pairs with modified method.

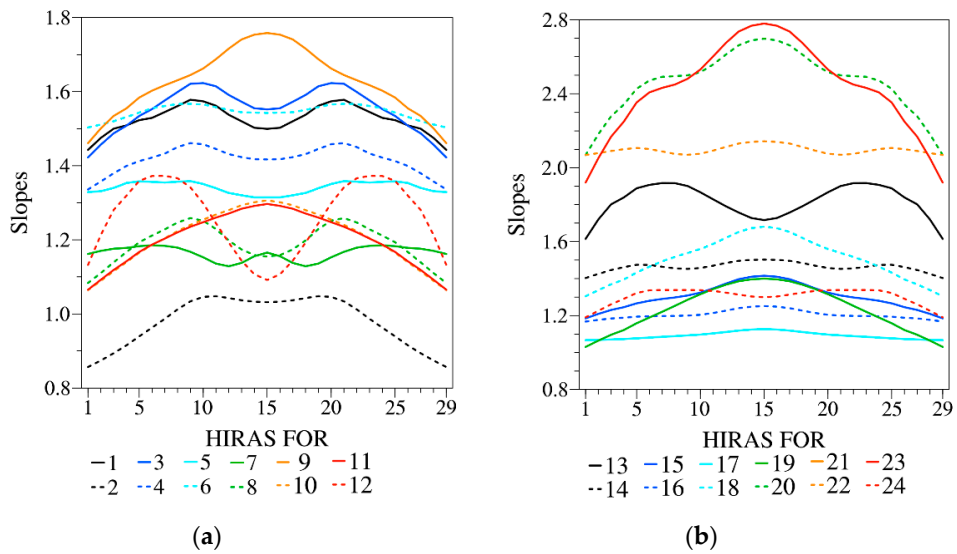


**Figure 11.** Cont.

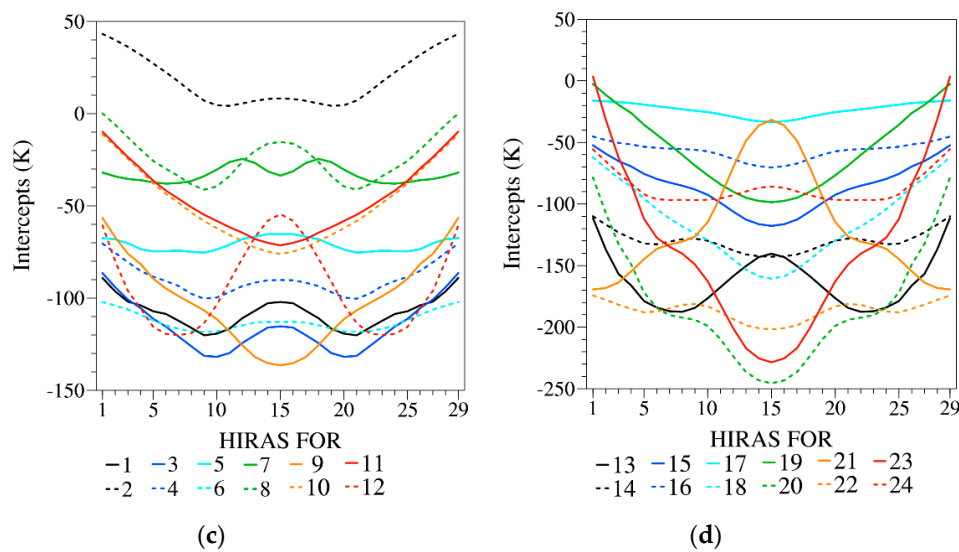


**Figure 11.** Regression coefficients (a,b)  $\alpha$  and (c,d)  $\beta$  of the linear regression model ( $T_{b,regression}^{SWIR} = \alpha T_{obs}^{LWIR} + \beta$ ) for 29 FORs of the 24 pairs with original method.

To illustrate the effectiveness of this improved cloud detection scheme proposed for HIRAS, cloud products from the AIRS onboard the Aqua satellite are used in this study. In the past few decades, the AIRS science team has made great achievements in cloud product retrievals from AIRS and the advanced microwave sounding unit instrument suite [33]. Ice cloud optical depth and cloud top pressure from the AIRS (version 6) products are used in this study because CESIs can well reflect the ice water content in the atmosphere and AIRS cloud products are particularly well suited to revealing valuable information about cloud altitudes [34].

Due to HIRAS observations in higher latitudes are affected by noise, the linear regression relationship between LWIR and SWIR brightness temperature is not very ideal. This study is conducted only over the tropics (30° S–30° N). Figure 12 shows the tropical distributions of AIRS ice cloud optical depth (Figure 12a) and cloud-top pressure (Figure 12b) during the daytime on 2 February 2019. We can see that clouds with high cloud-top pressures (above 400 hPa) are mainly concentrated in 20° S–20° N and ice water are mainly found in these high-altitude clouds. Comparing the distributions of two CESIs by modified method (MM) shown in Figure 12c,d, CESI<sup>MM</sup>-26 can capture features in the distributions of AIRS ice cloud optical depth better than CESI<sup>MM</sup>-6. That’s because different CESIs located at different peak WF heights and cloud-sensitive levels provide cloud information within different layers of the atmosphere. The AIRS ice cloud optical depth represents the clouds contained in all layers of atmosphere and CESI<sup>MM</sup>-26 reflects the clouds above 765 hPa. But CESI<sup>MM</sup>-6 can only provide information of clouds above 321 hPa. This explains why Figure 12a,d are more consistent.

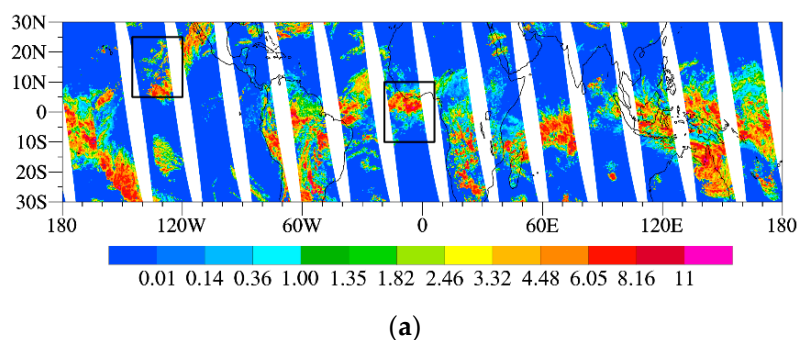


**Figure 12.** Cont.

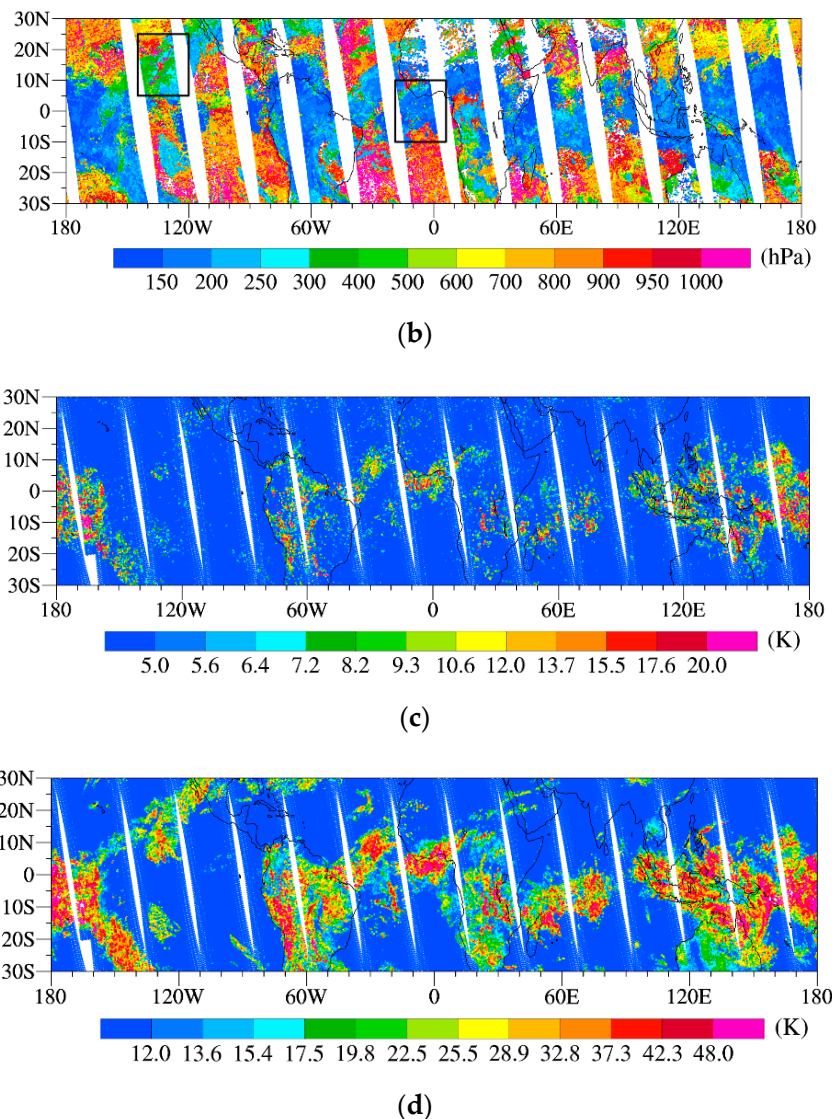
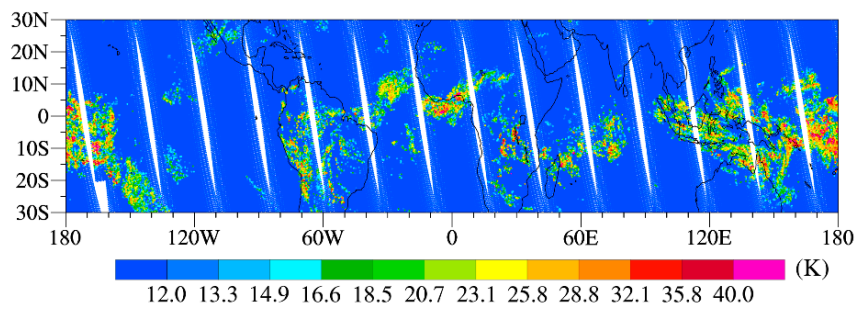
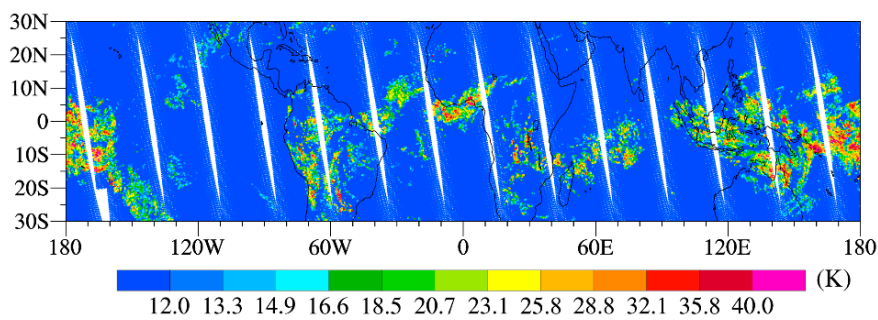


**Figure 12.** Spatial distributions of (a) AIRS ice cloud optical depth (color interval for  $\ln(\text{optical depth})$  is 0.3), (b) AIRS cloud-top pressure, (c)  $\text{CESI}^{\text{MM}-6}$  ( $\sim 321$  hPa) and (d)  $\text{CESI}^{\text{MM}-26}$  ( $\sim 765$  hPa) at ascending nodes on 2 February 2019. Color interval for  $\ln(\text{CESI})$  is 0.126.

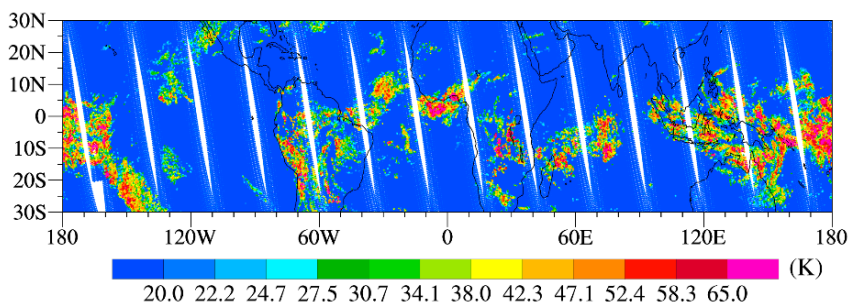
Next, we take a few more CESIs as examples to compare the cloud detection effects of the modified and original method (OM).  $\text{CESI}^{\text{MM}-21}$  and  $\text{CESI}^{\text{OM}-19}$ : Though the peak WFs of them are both located around 628 hPa, the WF broadness differences of them are quite different (Figure 7). We can explore the influence of WF broadness difference on cloud detection from comparison of these two CESIs.  $\text{CESI}^{\text{MM}-24}$  and  $\text{CESI}^{\text{OM}-22}$ : Their WF broadness differences are very close, and the only difference between them is that their paired SWIR channels are different (SWIR 2035 and SWIR 2031). For one LWIR channel, we can study the influence of different paired SWIR channels on cloud detection effects. Figure 13 shows the distributions of 4 CESIs above during the daytime on 2 February 2019. Obviously,  $\text{CESI}^{\text{MM}}$ s obtained by modified method (Figure 13c,d) can capture more features of cloud than original method (Figure 13a,b). The distributions of  $\text{CESI}^{\text{MM}}$  are more consistent with AIRS ice cloud optical depth and can give a more detailed description of the cloud distributions.



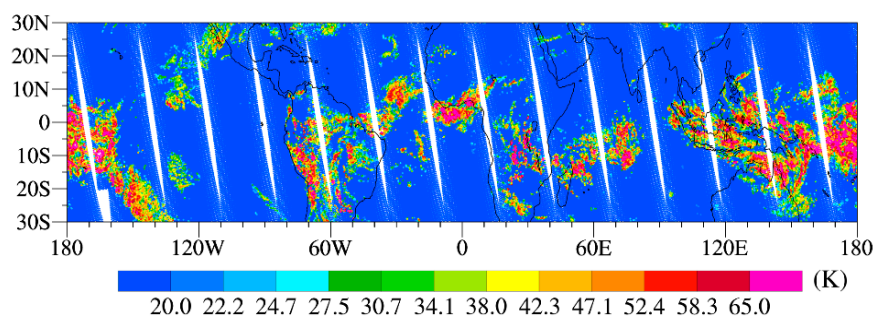
(a)



(b)



(c)



(d)

**Figure 13.** Spatial distributions of (a)  $\text{CESI}^{\text{OM}}_{19}$  (~628 hPa), (b)  $\text{CESI}^{\text{OM}}_{22}$  (~718 hPa), (c)  $\text{CESI}^{\text{MM}}_{21}$  (~628 hPa) and (d)  $\text{CESI}^{\text{MM}}_{24}$  (~718 hPa) at ascending nodes on 2 February 2019. Color interval for  $\ln(\text{CESI})$  is 0.126.

To show the distributions of  $\text{CESI}^{\text{MM}}$  and  $\text{CESI}^{\text{OM}}$  in more detail, we select data from two smaller areas (black boxes in Figure 12a,b) to compare by drawing them into scatter plots. Figure 14 shows the scatter plots of  $\text{CESI}^{\text{MM}}$  versus  $\text{CESI}^{\text{OM}}$  from the AIRS/HIRAS overlapping area over the two domains mentioned above with colors indicating the AIRS ice cloud optical depth. It can be seen that when there are few ice particles in the atmosphere, values of all these CESIs are close zero. In other words, CESIs are insensitive to clear sky. In general, as the amount of ice particle increases, so do values of CESIs. However, there are quite a few ice clouds that could be captured by  $\text{CESI}^{\text{MM}}$ s but show no reaction in  $\text{CESI}^{\text{OM}}$ s (circles scattering to the right). The same phenomenon exists in Figure 15. Both  $\text{CESI}^{\text{MM}}$  and  $\text{CESI}^{\text{OM}}$  show no reaction to the clouds near the surface (dark red circles). But when it comes to the upper atmosphere,  $\text{CESI}^{\text{MM}}$ s can capture more features of ice clouds with high cloud-top pressure than  $\text{CESI}^{\text{OM}}$ s (blue circles scattering to the right). According to the discussions above, the improved cloud detection scheme developed in this study can capture features in the distributions of AIRS-retrieved ice cloud optical depth and cloud-top pressure better than the original method.

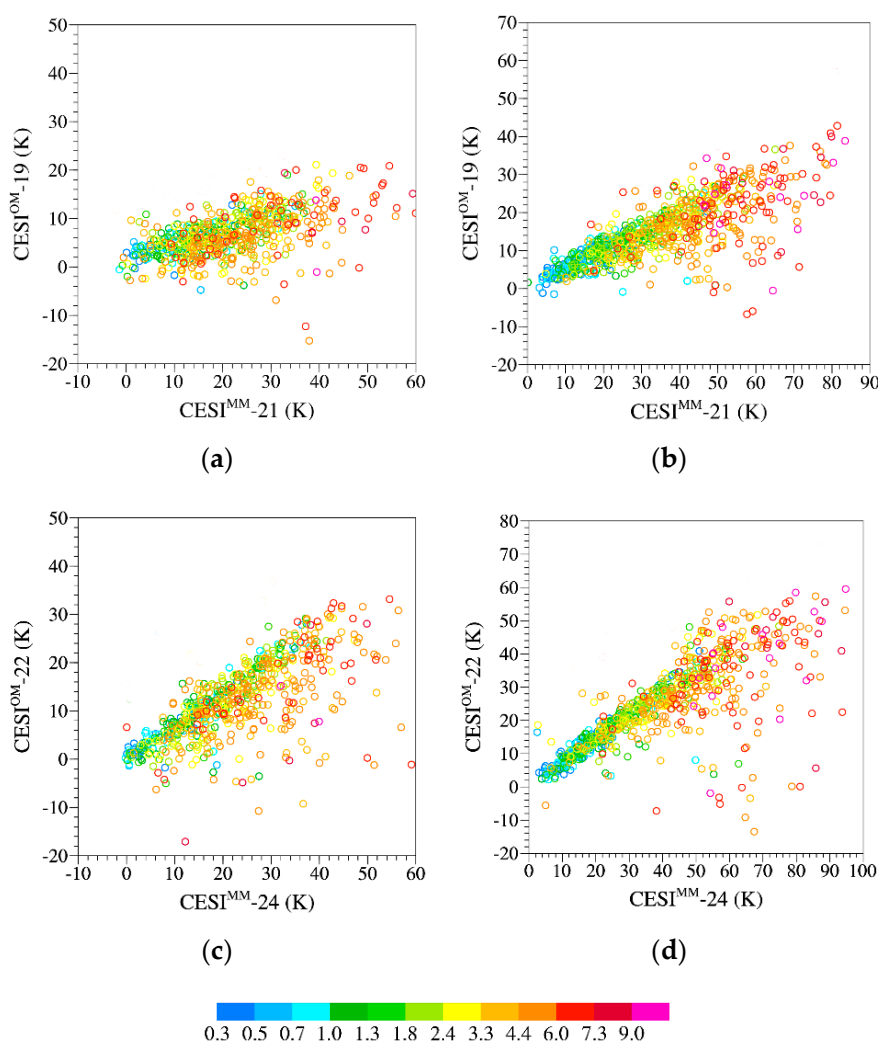


**Figure 14.** Scatter plots of (a,b)  $\text{CESI}^{\text{MM}}_{-21}$  versus  $\text{CESI}^{\text{OM}}_{-19}$  (~628 hPa) and (c,d)  $\text{CESI}^{\text{MM}}_{-24}$  versus  $\text{CESI}^{\text{OM}}_{-22}$  (~718 hPa) from the AIRS/HIRAS overlapping area at ascending nodes over domain 1 (left panels) and domain 2 (right panels) on 2 February 2019. The colors indicate AIRS ice cloud optical depth (Figure 12a).

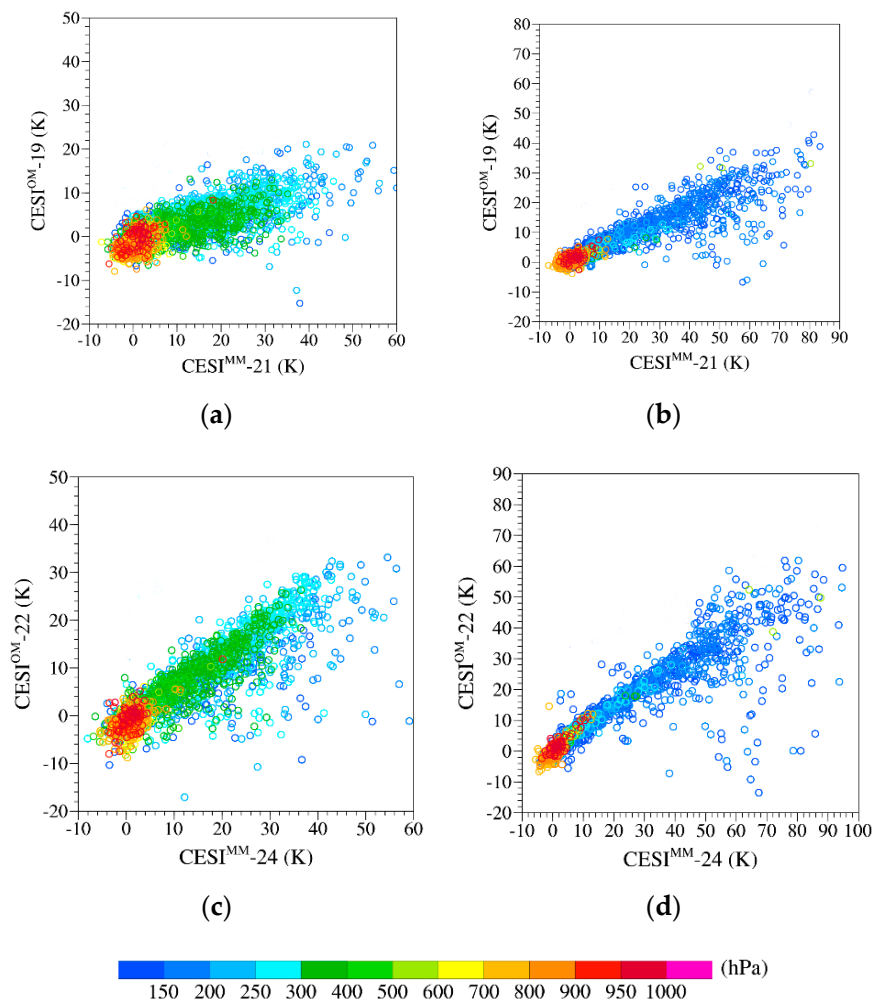


**Figure 15.** Scatter plots of (a,b) CEST<sup>MM</sup>-21 versus CEST<sup>OM</sup>-19 (~628 hPa) and (c,d) CEST<sup>MM</sup>-24 versus CEST<sup>OM</sup>-22 (~718 hPa) from the AIRS/HIRAS overlapping area at ascending nodes over domain 1 (left panels) and domain 2 (right panels) on 2 February 2019. The colors indicate AIRS ice cloud top pressure (Figure 12b).

## 5. Discussion

The improved cloud detection scheme developed in this study can capture features of ice clouds better than the original method. By adding more restrictions, the sensitivities to clouds of paired LWIR/SWIR channels are more similar and this method has more advantages in the identification of cloud height. However, this cloud detection scheme still has some shortcomings: (1) For now it can only be used for cloud detection over tropics when applied to HIRAS; (2) The determination of clear-sky thresholds for CESIs is a difficult problem. Once the CESI thresholds are determined, the modified CESIs could thus be used for cloud detection when assimilating HIRAS data for NWP. Our future research will focus on the determination of CESI thresholds for selecting clear-sky HIRAS data, bias estimates of HIRAS observations under clear-sky conditions, and assimilation of HIRAS data in the Global/Regional Assimilation and Prediction Enhanced System model.

## 6. Conclusions

The FY-3D HIRAS is the first Chinese operational hyperspectral infrared sounder providing high spectral resolution data for weather applications. It represents a major step forward in Chinese infrared sounding development. An improved cloud detection scheme using brightness temperature

observations from paired HIRAS LWIR and SWIR channels is developed here. When pairing LWIR and SWIR channels, the concept of WF broadness is proposed as an additional criterion to find LWIR and SWIR channels with similar WF peak altitudes. A set of height-dependent thresholds for differences of the cloud-sensitive levels between LWIR and SWIR channels is obtained and used for pairing. Before calculating the CESIs of the paired LWIR/SWIR channels, HIRAS clear-sky brightness temperature observations derived by collocating with MODIS cloud mask products are used for developing the linear regression models for all selected pairs. This approach avoids the simulation errors caused by profiles and ensures a sufficient amount of data for regression. The CESIs for the 26 (modified method) and 24 (original method) pairs are applied to HIRAS observations and compared with AIRS cloud products. The variations in CESIs in the lower atmosphere are consistent with ice water contents at all altitudes, and CESIs with higher peak WFs are sensitive to ice clouds in the upper troposphere. In the future, our research will focus on the determination of CESI thresholds for selecting clear-sky HIRAS data for NWP assimilation.

**Author Contributions:** Conceptualization, X.Z. and X.X.; methodology, X.Z.; software, X.X.; validation, X.X. and X.Z.; formal analysis, X.X.; investigation, X.X.; resources, X.Z.; data curation, X.X.; writing—original draft preparation, X.X.; writing—review and editing, X.X.; visualization, X.X.; supervision, X.Z.; project administration, X.Z.; funding acquisition, X.Z. All authors have read and agreed to the published version of the manuscript.

**Funding:** This research was funded by the National Key R&D Program of China (Grant 2018YFC1507004), special fund for the development of China Meteorological Administration numerical weather prediction systems (GRAPES), and the Postgraduate Research and Practice Innovation Program of Jiangsu Province (Grant KYCX20\_0916).

**Acknowledgments:** We would like to acknowledge the suggestions given by reviewers and editor.

**Conflicts of Interest:** We declared that we have no conflict of interest to this work. We declare that we do not have any commercial or associative interest that represents a conflict of interest in connection with the work submitted.

## References

1. Aumann, H.H.; Gregorich, D.T.; Gaiser, S.L.; Chahine, M.T. Application of Atmospheric Infrared Sounder (AIRS) data to climate research. *Proc. SPIE Int. Soc. Opt. Eng.* **2004**, *5570*, 202–208.
2. Blumstein, D.; Tournier, B.; Cayla, F.R.; Phulpin, T.; Fjortoft, R.; Buil, C.; Ponce, G. In-flight performance of the infrared atmospheric sounding interferometer (IASI) on METOP-A. *Proc. SPIE* **2007**, *6684*, 66840. [[CrossRef](#)]
3. Pougatchev, N.; August, T.; Calbet, X.; Hultberg, T.; Oduleye, O.; Schlüssel, P.; Stiller, B.; Germain, K.S.; Bingham, G. IASI temperature and water vapor retrievals—Error assessment and validation. *Atmos. Chem. Phys. Discuss.* **2009**, *9*, 6453–6458. [[CrossRef](#)]
4. Aumann, H.; Chahine, M.; Gautier, C.; Goldberg, M.; Kalnay, E.; McMillin, L.; Revercomb, H.; Rosenkranz, P.; Smith, W.; Staelin, D.; et al. AIRS/AMSU/HSB on the aqua mission: Design, science objectives, data products, and processing systems. *IEEE Trans. Geosci. Remote Sens.* **2003**, *41*, 253–264. [[CrossRef](#)]
5. Klaes, K.D.; Cohen, M.; Buhler, Y.; Schlüssel, P.; Munro, R.; Luntama, J.-P.; Von Engeln, A.; Clérigh, E.Ó.; Bonekamp, H.; Ackermann, J.; et al. An Introduction to the EUMETSAT Polar system. *Bull. Am. Meteorol. Soc.* **2007**, *88*, 1085–1096. [[CrossRef](#)]
6. Hilton, F.; Armante, R.; August, T.; Barnet, C.; Bouchard, A.; Camy-Peyret, C.; Capelle, V.; Clarisse, L.; Clerbaux, C.; Coheur, P.-F.; et al. Hyperspectral Earth Observation from IASI: Five Years of Accomplishments. *Bull. Am. Meteorol. Soc.* **2012**, *93*, 347–370. [[CrossRef](#)]
7. Han, Y.; Revercomb, H.E.; Crompton, M.; Gu, D.; Johnson, D.B.; Mooney, D.; Scott, D.; Strow, L.L.; Bingham, G.E.; Borg, L.; et al. Suomi NPP CrIS measurements, sensor data record algorithm, calibration and validation activities, and record data quality. *J. Geophys. Res. Atmos.* **2013**, *118*, 12734–12738. [[CrossRef](#)]
8. Carminati, F.; Xiao, X.; Lu, Q.; Atkinson, N.; Hocking, J. Assessment of the Hyperspectral Infrared Atmospheric Sounder (HIRAS). *Remote Sens.* **2019**, *11*, 2950. [[CrossRef](#)]
9. Qi, C.; Wu, C.; Hu, X.; Xu, H.; Lee, L.; Zhou, F.; Gu, M.; Yang, T.; Shao, C.; Yang, Z.; et al. High Spectral Infrared Atmospheric Sounder (HIRAS): System Overview and On-Orbit Performance Assessment. *IEEE Trans. Geosci. Remote Sens.* **2020**, *58*, 4335–4352. [[CrossRef](#)]
10. Wu, C.; Qi, C.; Hu, X.; Gu, M.; Yang, T.; Xu, H.; Lee, L.; Yang, Z.; Zhang, P. FY-3D HIRAS Radiometric Calibration and Accuracy Assessment. *IEEE Trans. Geosci. Remote Sens.* **2020**, *58*, 3965–3976. [[CrossRef](#)]

11. Hilton, F.; Atkinson, N.C.; English, S.J.; Eyre, J.R. Assimilation of IASI at the Met Office and assessment of its impact through observing system experiments. *Q. J. R. Meteorol. Soc.* **2009**, *135*, 495–505. [[CrossRef](#)]
12. McNally, A.P.; Watts, P.D.; Smith, J.A.; Engelen, R.; Kelly, G.A.; Thépaut, J.N.; Matricardi, M. The assimilation of AIRS radiance data at ECMWF. *Q. J. R. Meteorol. Soc.* **2006**, *132*, 935–957. [[CrossRef](#)]
13. Li, Z.; Shen, H.; Wei, Y.; Cheng, Q.; Yuan, Q. Cloud detection by fusing multi-scale convolutional features. *ISPRS Ann. Photogramm. Remote Sens. Spat. Inf. Sci.* **2018**, *IV3*, 149–152. [[CrossRef](#)]
14. Wu, X.; Pan, B. Utilizing Multilevel Features for Cloud Detection on Satellite Imagery. *Remote Sens.* **2018**, *10*, 1853. [[CrossRef](#)]
15. Mahajan, S.; Fataniya, B. Cloud detection methodologies: Variants and development—A review. *Complex Intell. Syst.* **2020**, *6*, 251–261. [[CrossRef](#)]
16. Amato, U.; Lavanant, L.; Liuzzi, G.M.; Masiello, G.; Serio, C.; Stuhlmann, R.; Tjemkes, S. Cloud mask via cumulative discriminant analysis applied to satellite infrared observations: Scientific basis and initial evaluation. *Atmos. Meas. Tech.* **2014**, *7*, 3355–3372. [[CrossRef](#)]
17. Saunders, R.W.; Kriebel, K.T. An improved method for detecting clear sky and cloudy radiances from AVHRR data. *Int. J. Remote Sens.* **1988**, *9*, 123–150. [[CrossRef](#)]
18. Frey, R.A.; Ackerman, S.A.; Liu, Y.; Strabala, K.I.; Zhang, H.; Key, J.; Wang, X. Cloud Detection with MODIS. Part I: Improvements in the MODIS Cloud Mask for Collection 5. *J. Atmos. Ocean. Technol.* **2008**, *25*, 1057–1072. [[CrossRef](#)]
19. Kopp, T.J.; Thomas, W.; Heidinger, A.K.; Botambekov, D.; Frey, R.A.; Hutchison, K.D.; Iisager, B.D.; Brueske, K.; Reed, B. The VIIRS Cloud Mask: Progress in the first year of S-NPP toward a common cloud detection scheme. *J. Geophys. Res. Atmos.* **2014**, *119*, 2441–2456. [[CrossRef](#)]
20. McNally, A.P.; Watts, P.D. A cloud detection algorithm for high-spectral-resolution infrared sounders. *Q. J. R. Meteorol. Soc.* **2003**, *129*, 3411–3423. [[CrossRef](#)]
21. Menzel, W.P.; Schmit, T.J.; Zhang, P.; Li, J. Satellite-Based Atmospheric Infrared Sounder Development and Applications. *Bull. Am. Meteorol. Soc.* **2018**, *99*, 583–603. [[CrossRef](#)]
22. Smith, W.L.; Platt, C.M.R. Comparison of Satellite-Deduced Cloud Heights with Indications from Radiosonde and Ground-Based Laser Measurements. *J. Appl. Meteorol.* **1978**, *17*, 1796–1802. [[CrossRef](#)]
23. Wielicki, B.A.; Coakley, J.A. Cloud Retrieval Using Infrared Sounder Data: Error Analysis. *J. Appl. Meteorol.* **1981**, *20*, 157–169. [[CrossRef](#)]
24. Wylie, D.P.; Menzel, W.P.; Woolf, H.M.; Strabala, K.I. Four Years of Global Cirrus Cloud Statistics Using HIRS. *J. Clim.* **1995**, *7*, 1972–1986. [[CrossRef](#)]
25. Lin, L.; Qin, Z.; Weng, F. Combining CrIS double CO<sub>2</sub> bands for detecting clouds located in different layers of the atmosphere. *J. Geophys. Res. Atmos.* **2017**, *122*, 1811–1827. [[CrossRef](#)]
26. Aumann, H.H.; Chen, X.; Fishbein, E.; Geer, A.; Havemann, S.; Huang, X.; Liu, X.; Liuzzi, G.; DeSouza-Machado, S.; Manning, E.M.; et al. Evaluation of Radiative Transfer Models With Clouds. *J. Geophys. Res. Atmos.* **2018**, *123*, 6142–6157. [[CrossRef](#)]
27. Saunders, R.; Matricardi, M.; Brunel, P. An improved fast radiative transfer model for assimilation of satellite radiance observations. *Q. J. R. Meteorol. Soc.* **1999**, *125*, 1407–1425. [[CrossRef](#)]
28. Li, X.; Zou, X. Bias characterization of CrIS radiances at 399 selected channels with respect to NWP model simulations. *Atmos. Res.* **2017**, *196*, 164–181. [[CrossRef](#)]
29. Carrier, M.J.; Zou, X.; Lapenta, W.M. Identifying Cloud-Uncontaminated AIRS Spectra from Cloudy FOV Based on Cloud-Top Pressure and Weighting Functions. *Mon. Weather Rev.* **2007**, *135*, 2278–2294. [[CrossRef](#)]
30. Xu, L.; Fang, S.; Niu, R.; Li, J. Cloud detection based on decision tree over tibetan plateau with modis data. *ISPRS Int. Arch. Photogramm. Remote Sens. Spat. Inf. Sci.* **2012**, *1*, 535–538. [[CrossRef](#)]
31. Han, Y.; Qin, Z.; Weng, F. Cloud and precipitation features of Super Typhoon Neoguri revealed from dual oxygen absorption band sounding instruments on board FengYun-3C satellite. *Geophys. Res. Lett.* **2015**, *42*, 916–924. [[CrossRef](#)]
32. Saunders, R.; Hocking, J.; Turner, E.; Rayer, P.; Rundle, D.; Brunel, P.; Vidot, J.; Roquet, P.; Matricardi, M.; Geer, A.; et al. An update on the RTTOV fast radiative transfer model (currently at version 12). *Geosci. Model Dev.* **2018**, *11*, 2717–2737. [[CrossRef](#)]
33. Kahn, B.H.; Hanii, T.; Stephens, G.L.; Qing, Y.; Julien, D.; Gerald, M.; Manning, E.M.; Heymsfield, A.J. The Atmospheric Infrared Sounder. *Atmos. Chem. Phys.* **2018**, *18*, 10715–10739. [[CrossRef](#)]

34. Weisz, E.; Li, J.; Menzel, W.P.; Heidinger, A.K.; Kahn, B.H.; Liu, C.-Y. Comparison of AIRS, MODIS, CloudSat and CALIPSO cloud top height retrievals. *Geophys. Res. Lett.* **2007**, *34*, 17811. [[CrossRef](#)]

**Publisher's Note:** MDPI stays neutral with regard to jurisdictional claims in published maps and institutional affiliations.



© 2020 by the authors. Licensee MDPI, Basel, Switzerland. This article is an open access article distributed under the terms and conditions of the Creative Commons Attribution (CC BY) license (<http://creativecommons.org/licenses/by/4.0/>).